Supplement of The Cryosphere, 17, 327–348, 2023
https://doi.org/10.5194/tc-17-327-2023-supplement
© Author(s) 2023. CC BY 4.0 License.

The Cryosphere Open Access EGU

Supplement of

Timescales of outlet-glacier flow with negligible basal friction: theory, observations and modeling

Johannes Feldmann and Anders Levermann

Correspondence to: Johannes Feldmann (johannes.feldmann@pik-potsdam.de) and Anders Levermann (anders.levermann@pik-potsdam.de)

The copyright of individual parts of the supplement might differ from the article licence.

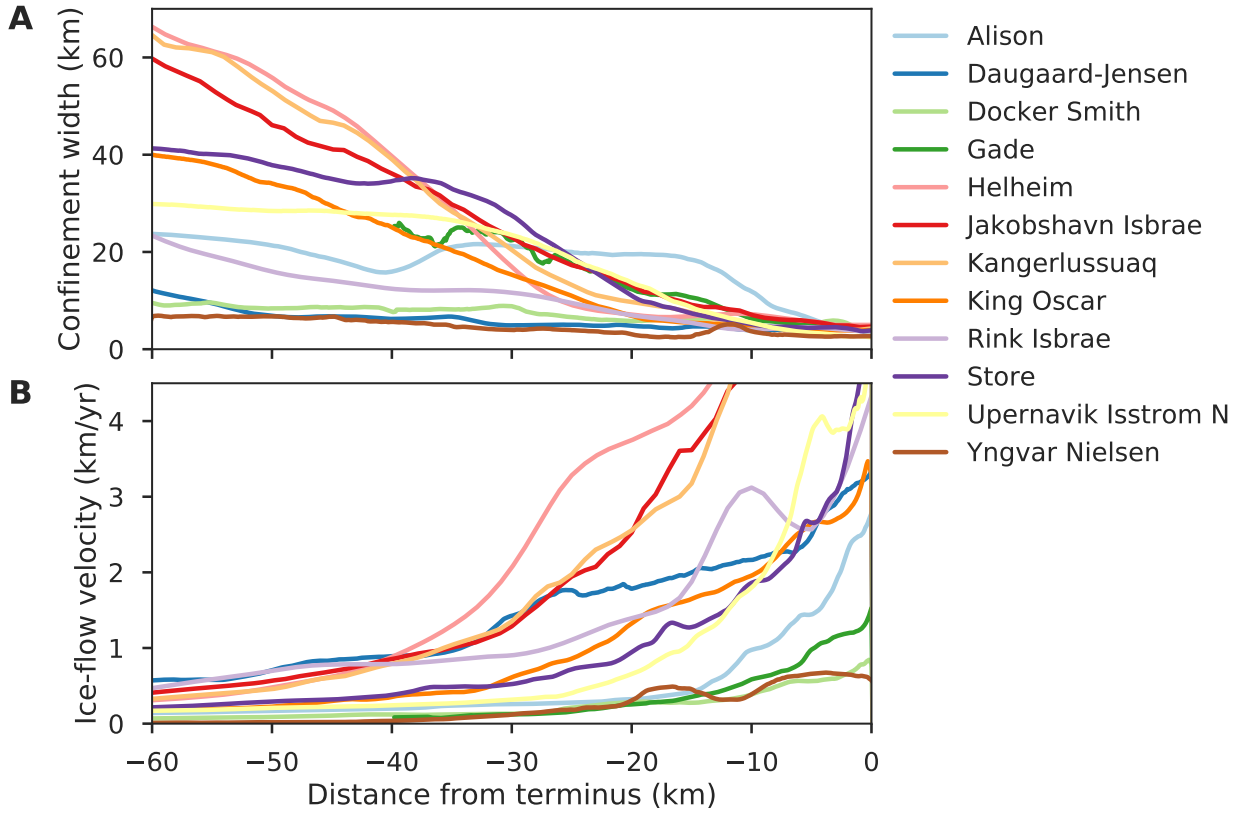

Figure S1. Comparison of observational data for (**A**) the confinement-width profiles and (**B**) the flow-speed profiles between the Greenland outlet glaciers from Beckmann et al. (2019) that we use in our scaling analysis.

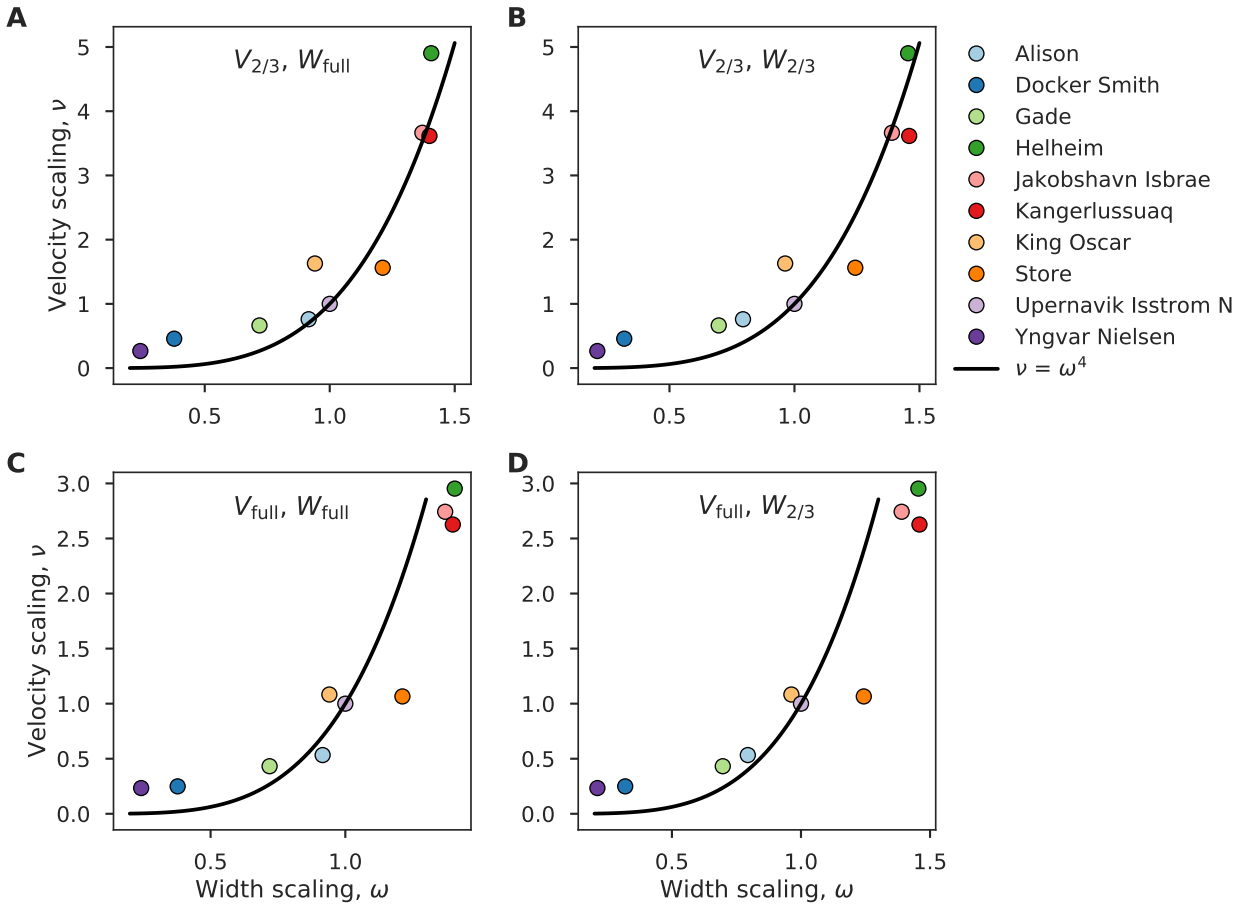

Figure S2. Comparison of scaling results for four different choices of the averaging ranges along the velocity and width profiles of the analyzed Greenland outlets. Panel **A** shows the result presented in the main manuscript (Sect. 3.1 and Fig. 3), which is based on the full range of the width profile (denoted by W_{full}) but neglects the ocean-ward third of the velocity profile (denoted by $V_{2/3}$). The other three panels show the results for the three other possible combinations of (not) excluding the ocean-ward third of the velocity and/or width profiles.

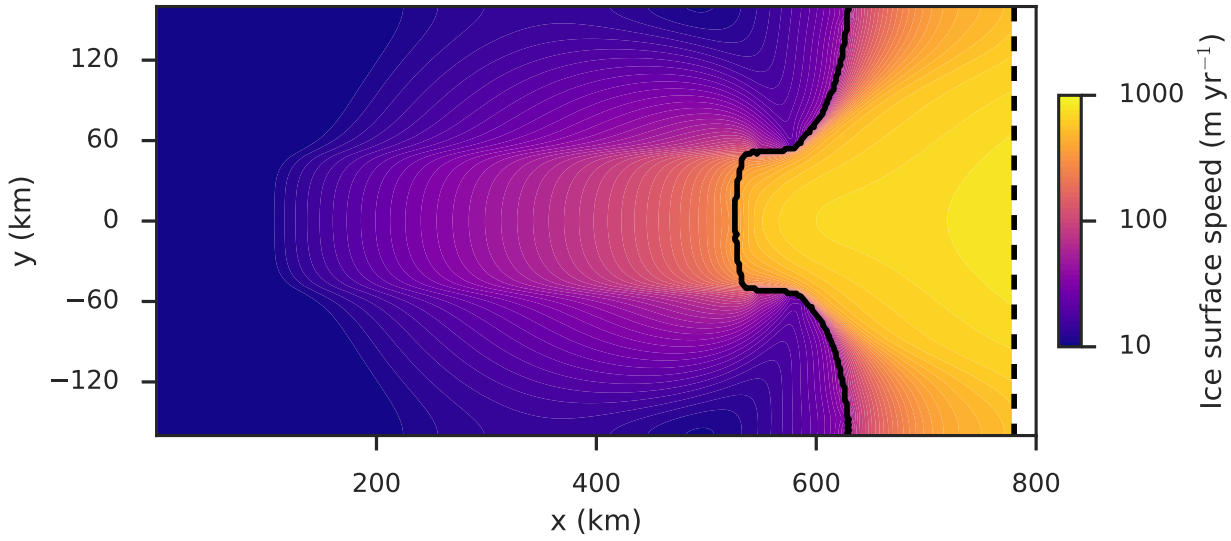

Figure S3. Magnitude of simulated ice surface velocity in equilibrium for a stable configuration ($W = 100$ km). Inside the bed confinement ice flow accelerates towards the ocean, forming an ice stream that feeds the downstream ice shelf. Thick grey contours indicate positions of grounding line (continuous) and fixed calving front (dashed).

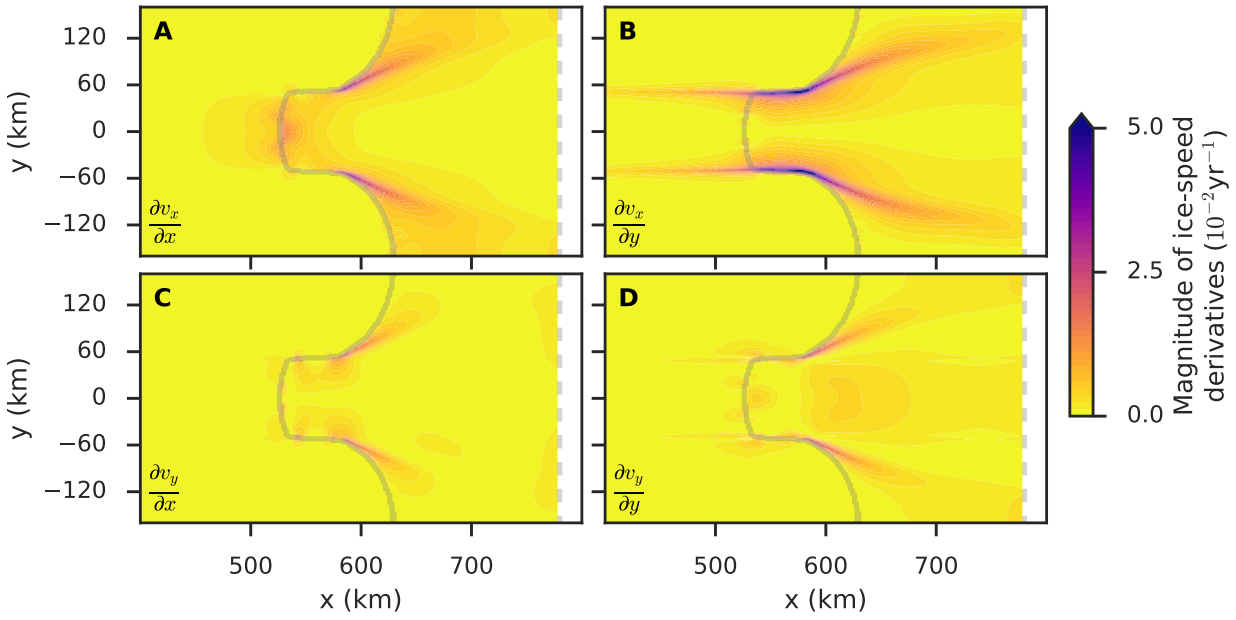

Figure S4. Magnitude of spatial derivatives in x and y directions of the ice-speed components v_x and v_y after equilibration of the simulated ice-sheet-shelf system in a stable configuration ($W = 100$ km). Grey contours indicate positions of grounding line (continuous) and fixed calving front (dashed).

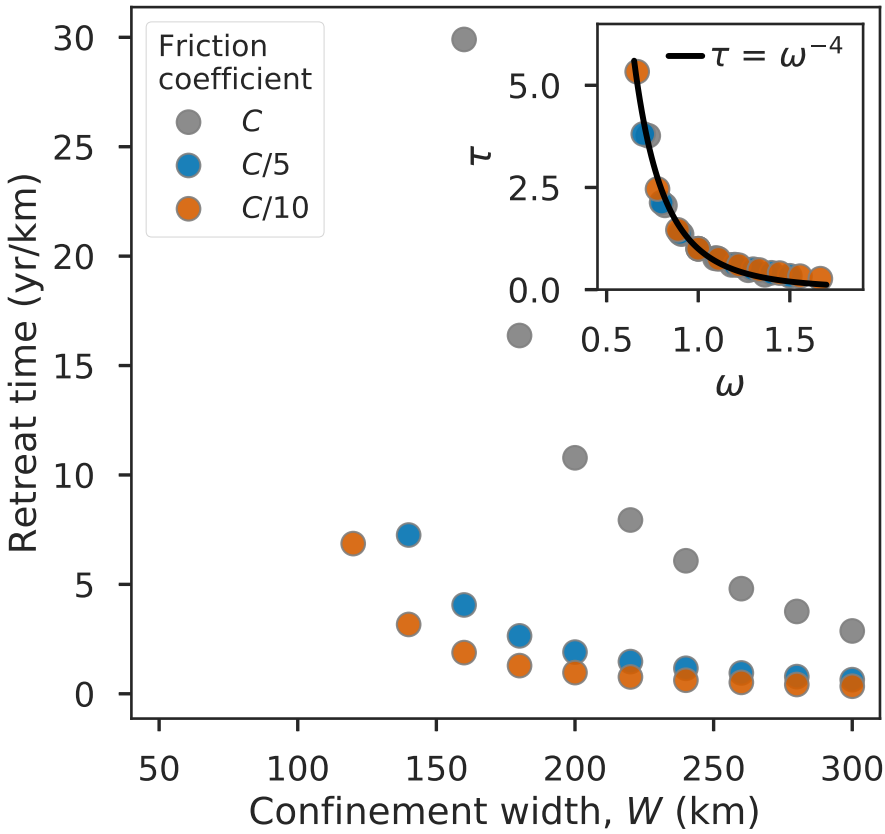

Figure S5. Time scaling of simulated unstable ice-sheet retreat. Characteristic retreat timescale T down the retrograde bed slope (measured in years per km of retreat) dependent on the width of the confinement and the basal friction coefficient C (legend). The inset shows the scaling if data is normed to a reference confinement width and the associated reference timescale. The black curves give the scaling behavior according to the analytically-derived scaling relation (Eq. 4).

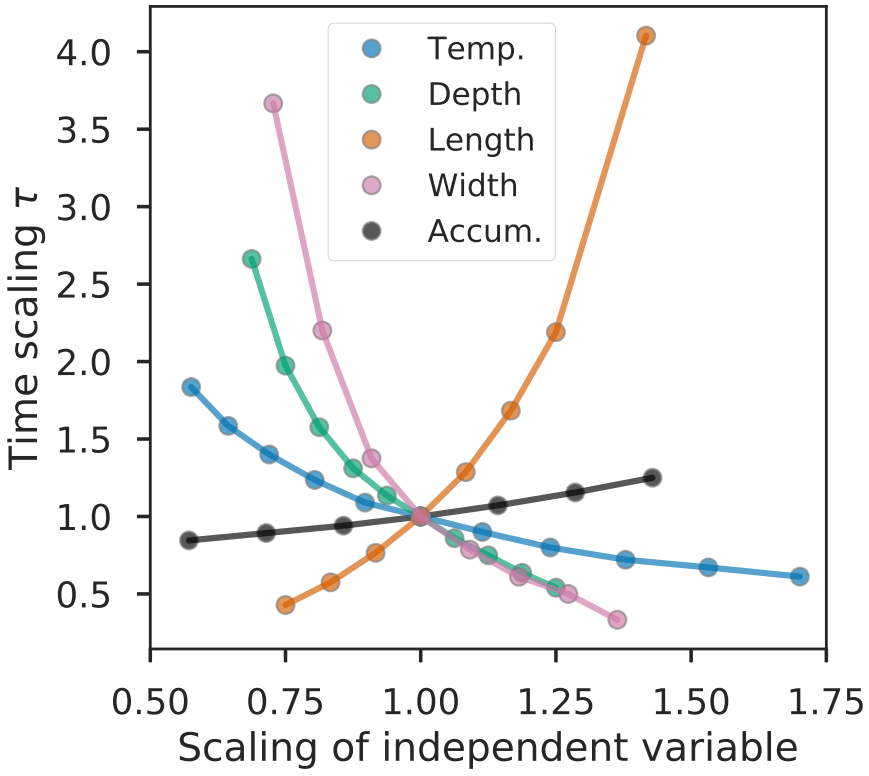

Figure S6. Time scaling of simulated unstable ice-sheet retreat dependent on the scaling of the ice softness, the depth of the confinement, the length of the confinement, the width of the confinement and the accumulation rate (legend).

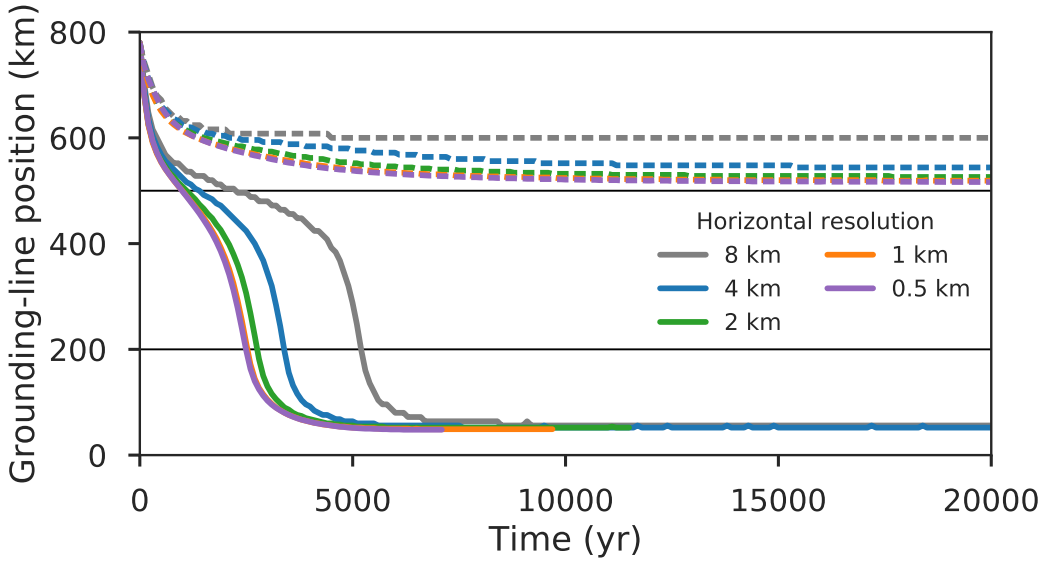

Figure S7. Convergence study of the centerline grounding-line evolution for a stable configuration ($W = 100$ km, dashed lines) and an unstable configuration ($W = 220$ km, continuous lines). The region between the two thin horizontal lines corresponds to the section of retrograde bed slope.

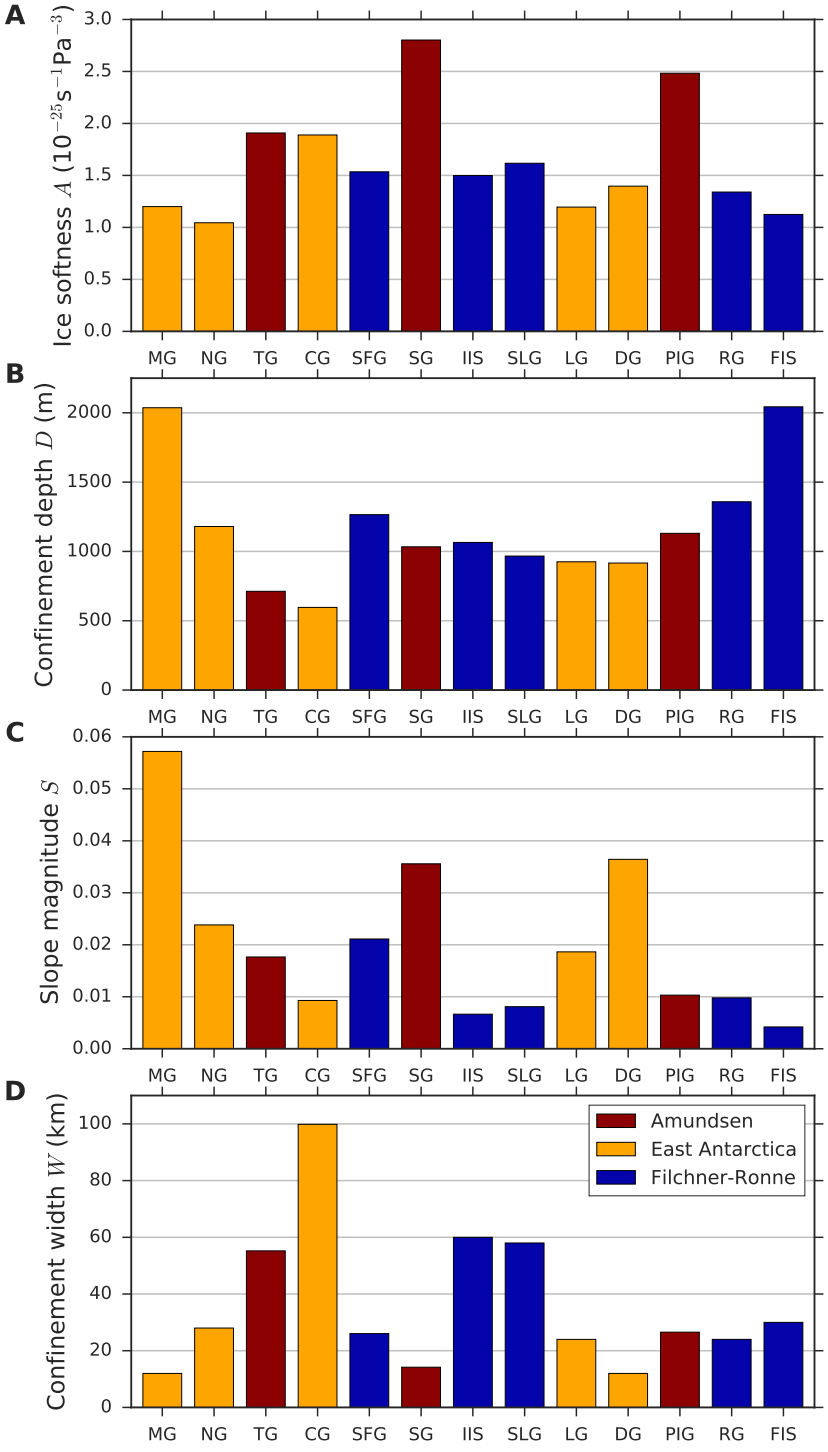

Figure S8. Median values of extracted characteristic scales for each outlet. **(A)** Ice softness, **(B)** confinement depth, **(C)** confinement length scale and **(D)** confinement width.

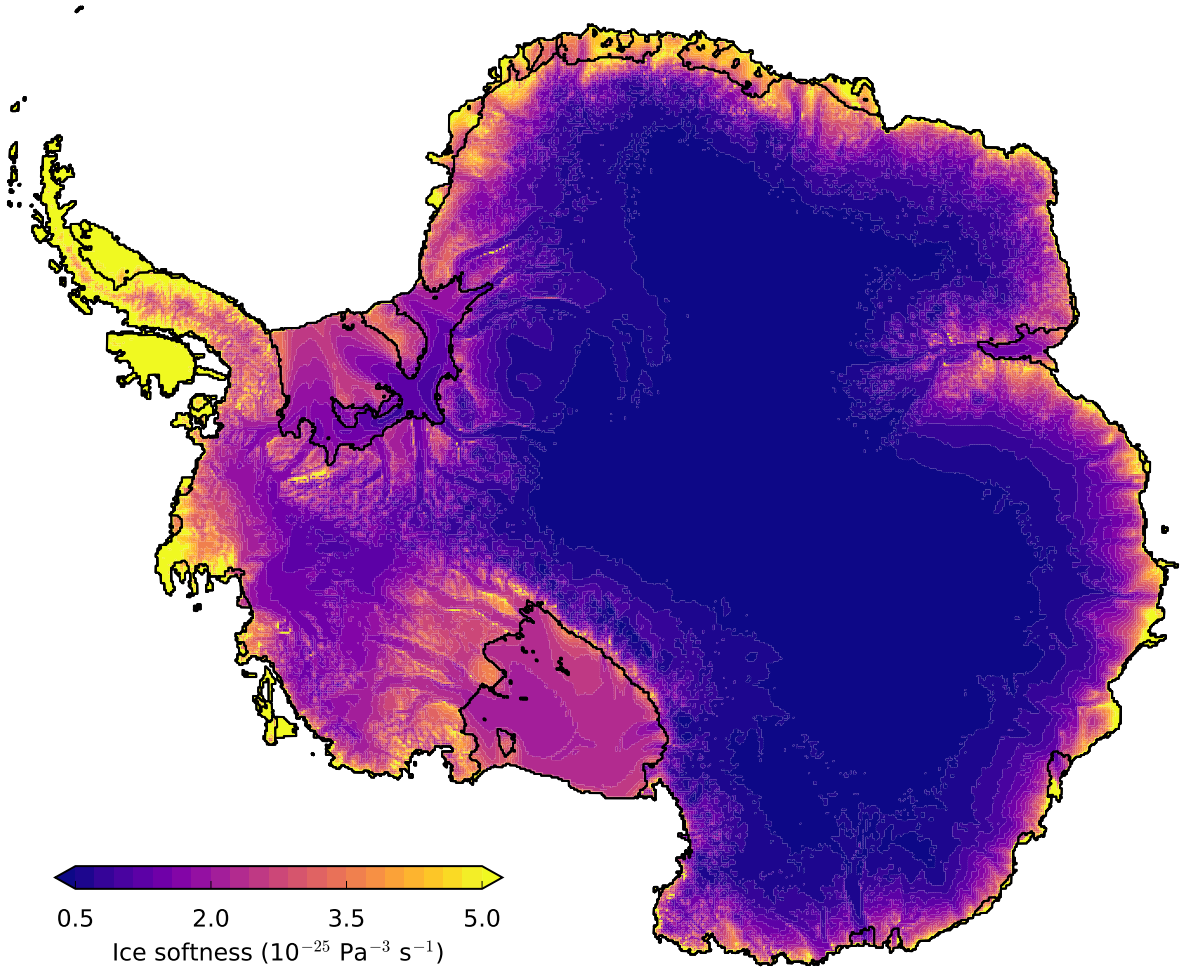

Figure S9. Vertically averaged Antarctic ice softness field from the ice sheet model PISM computed under present-day boundary conditions in the course of the recent ISMIP 6 Antarctica intercomparison project (Seroussi et al., 2020). Position of grounding line and calving front represented by black contours.

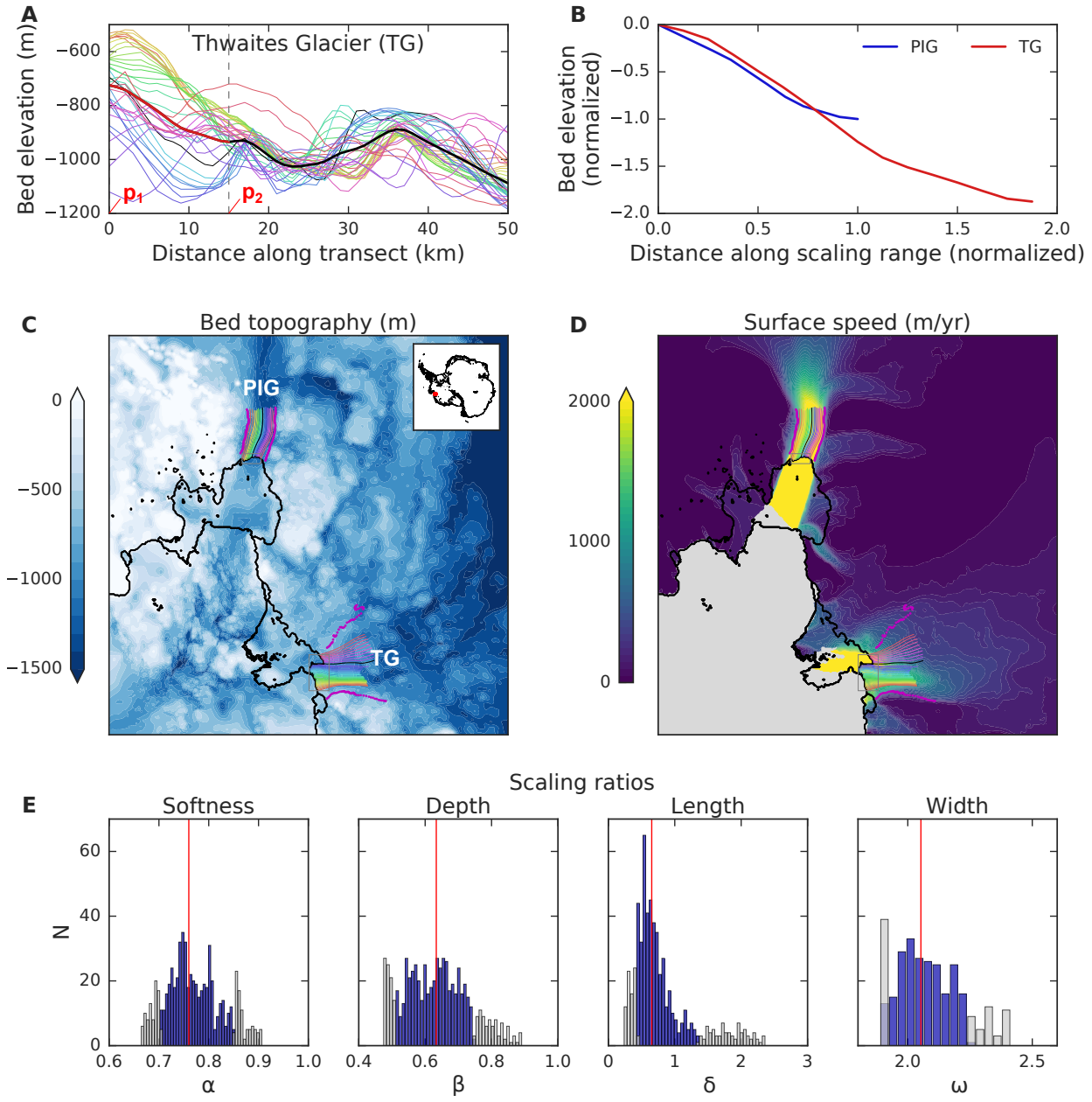

Figure S10. Data used to infer the scaling ratio distributions, forming the basis for our timescale calculation, shown for Thwaites Glacier (TG) with respect to the reference Pine Island Glacier (PIG). **(A)** Elevation of bedrock along the streamlines of the TG confinement (colors, see panels **(C)** and **(D)**) with flux-weighted average (thick black) and retrograde slope section (red) that is used to infer the outlet's characteristic vertical scale at location p_1 and the slope magnitude (length scale) between p_1 and p_2. **(B)** Flux-averaged bed geometry of TG's retrograde slope section from panel **(A)** (red), scaled with the respective length-scale ratio and normalized to the dimensions of PIG (blue), revealing the similarity of both slopes. Maps of **(C)** bed topography (Morlighem et al., 2020) and **(D)** surface velocity (Mouginot et al., 2019) with inferred streamlines (colored) and lateral confinement (magenta). **(E)** Distributions of the scaling ratios for the ice softness α, confinement depth β, confinement length δ and confinement width ω (5^{th} to 95^{th} percentiles; with likely range, i.e., 17^{th} to 83^{th} percentiles, highlighted in blue).

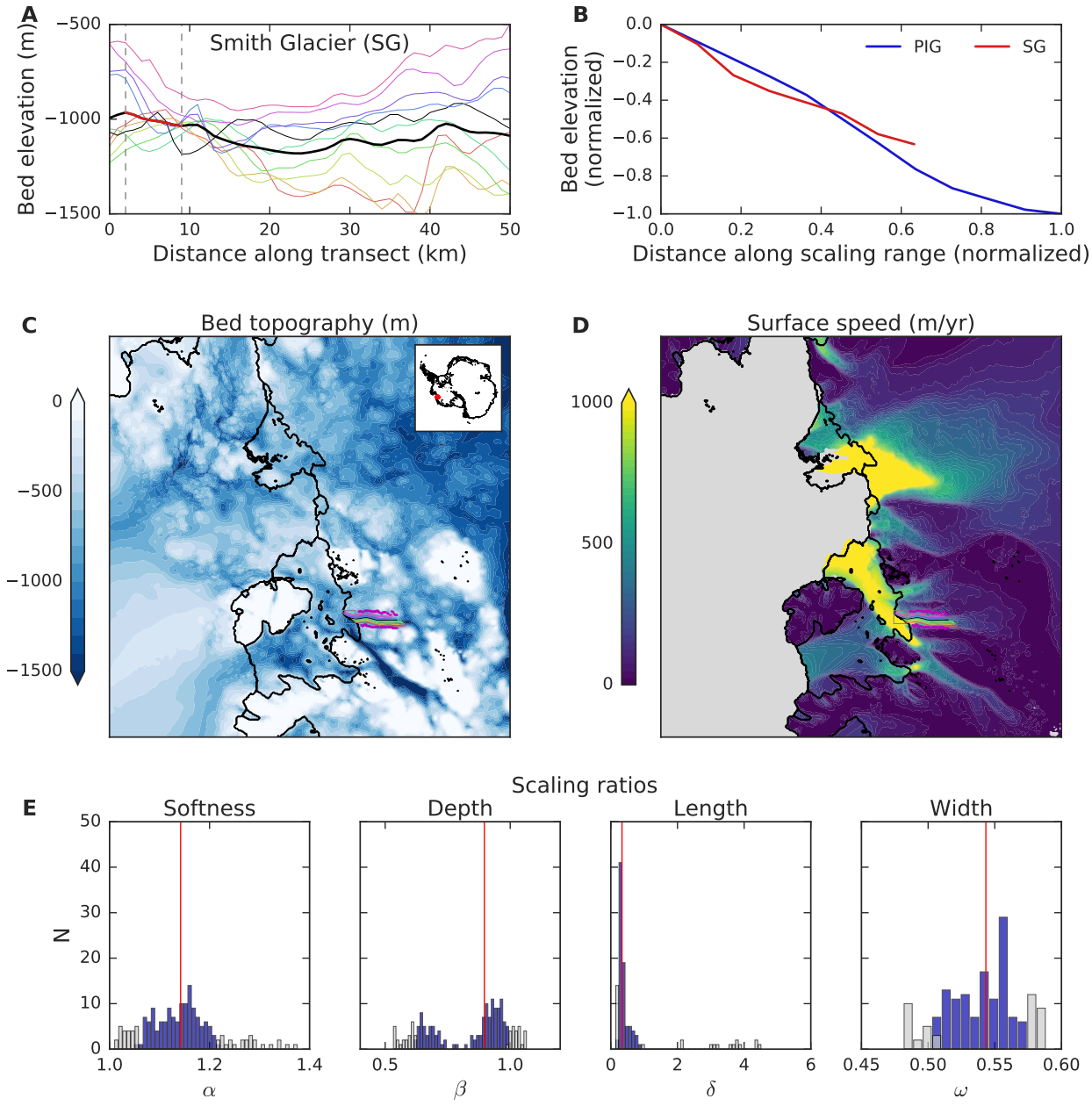

Figure S11. Same as Fig. S10, here for Smith Glacier (SG).

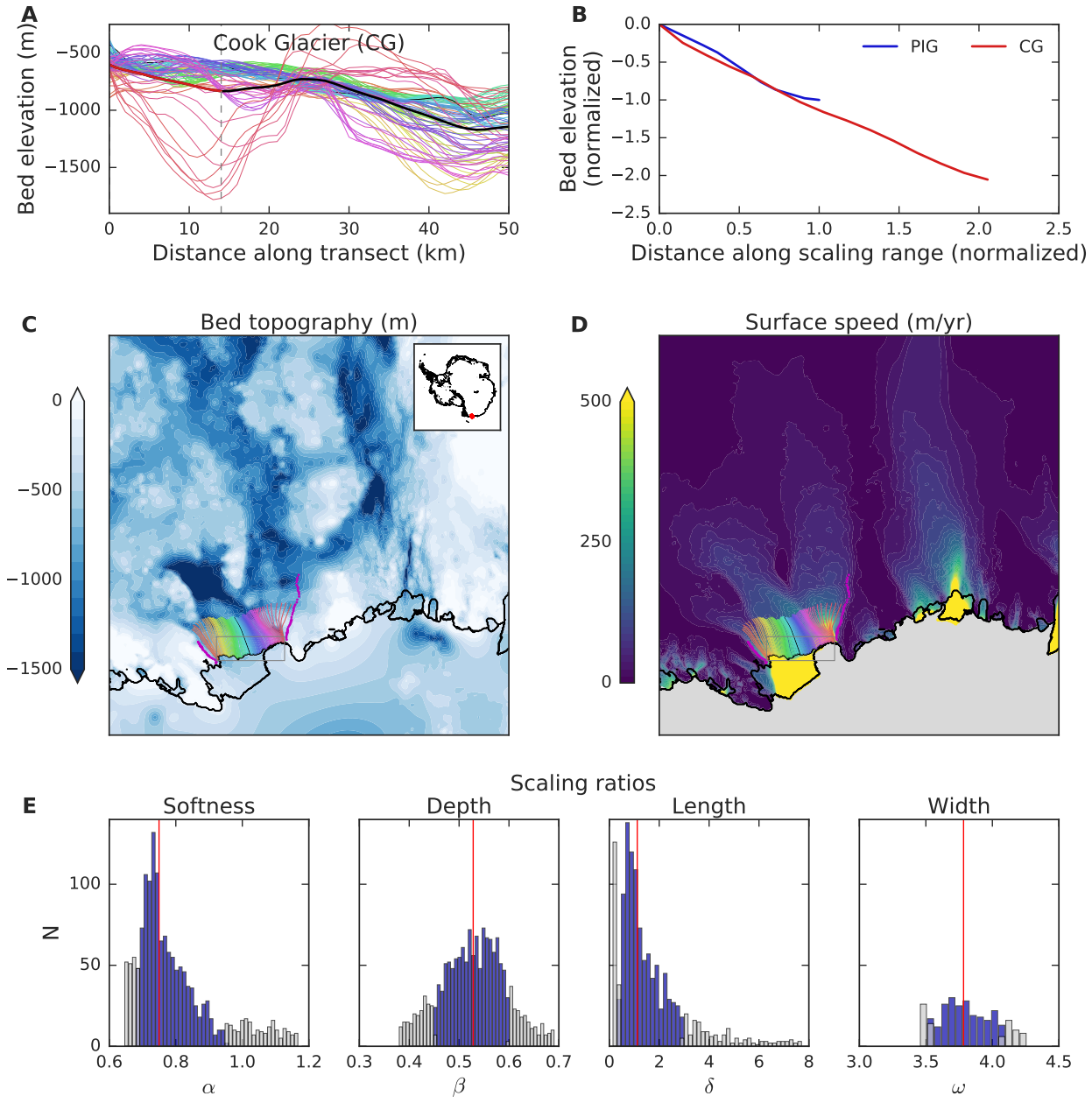

Figure S12. Same as Fig. S10, here for Cook Glacier (CG).

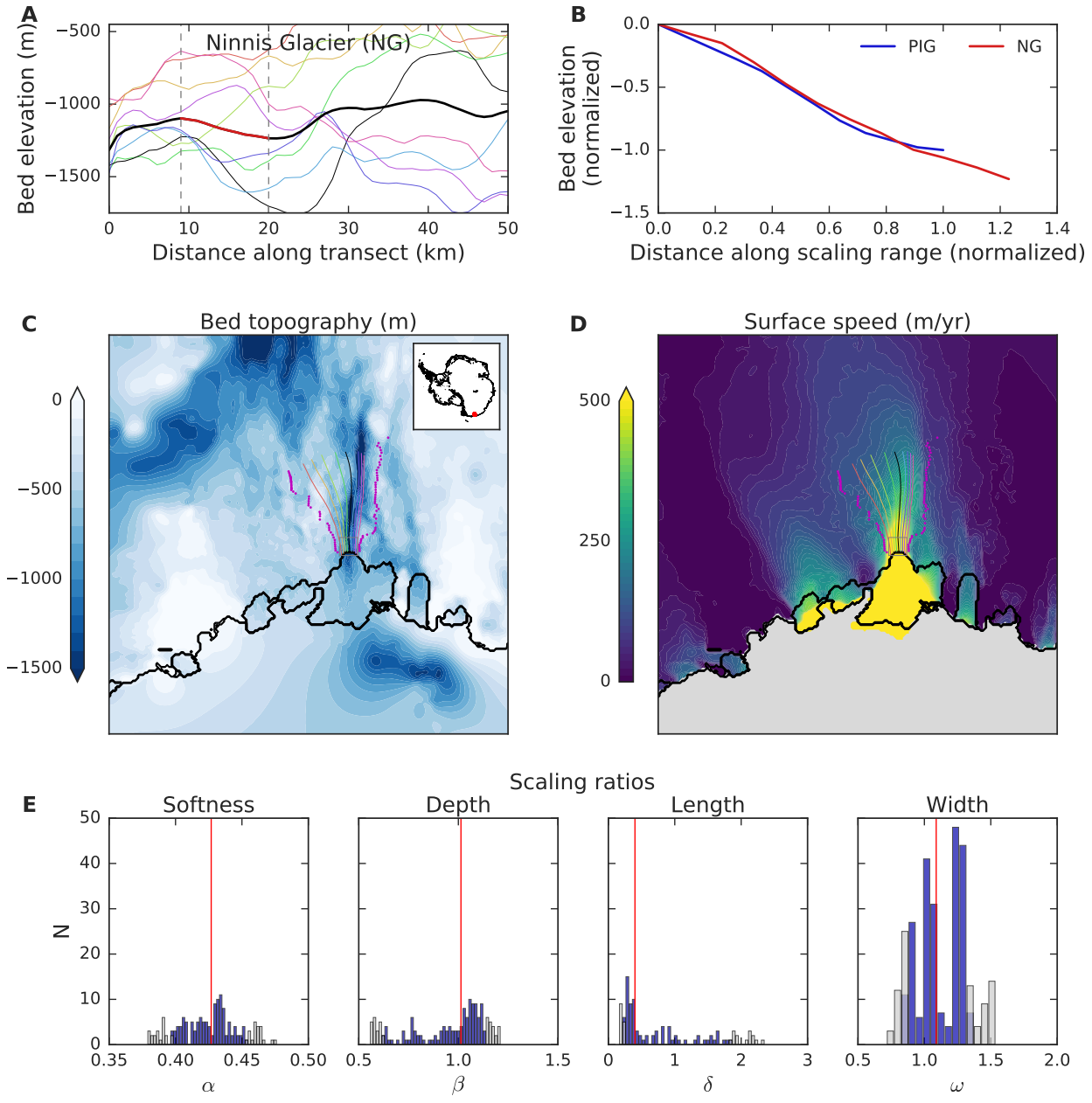

Figure S13. Same as Fig. S10, here for Ninnis Glacier (NG).

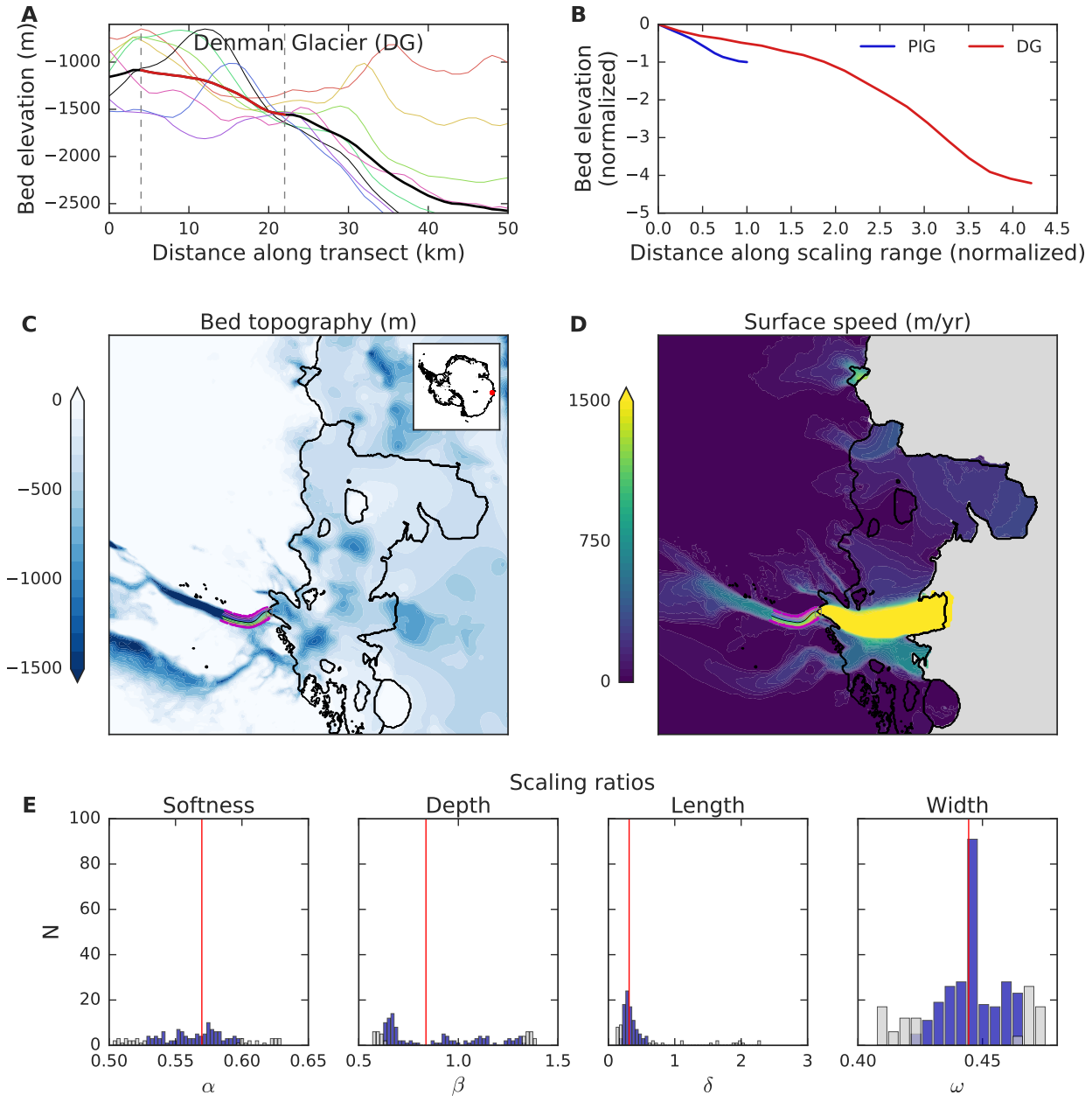

Figure S14. Same as Fig. S10, here for Denman Glacier (DG).

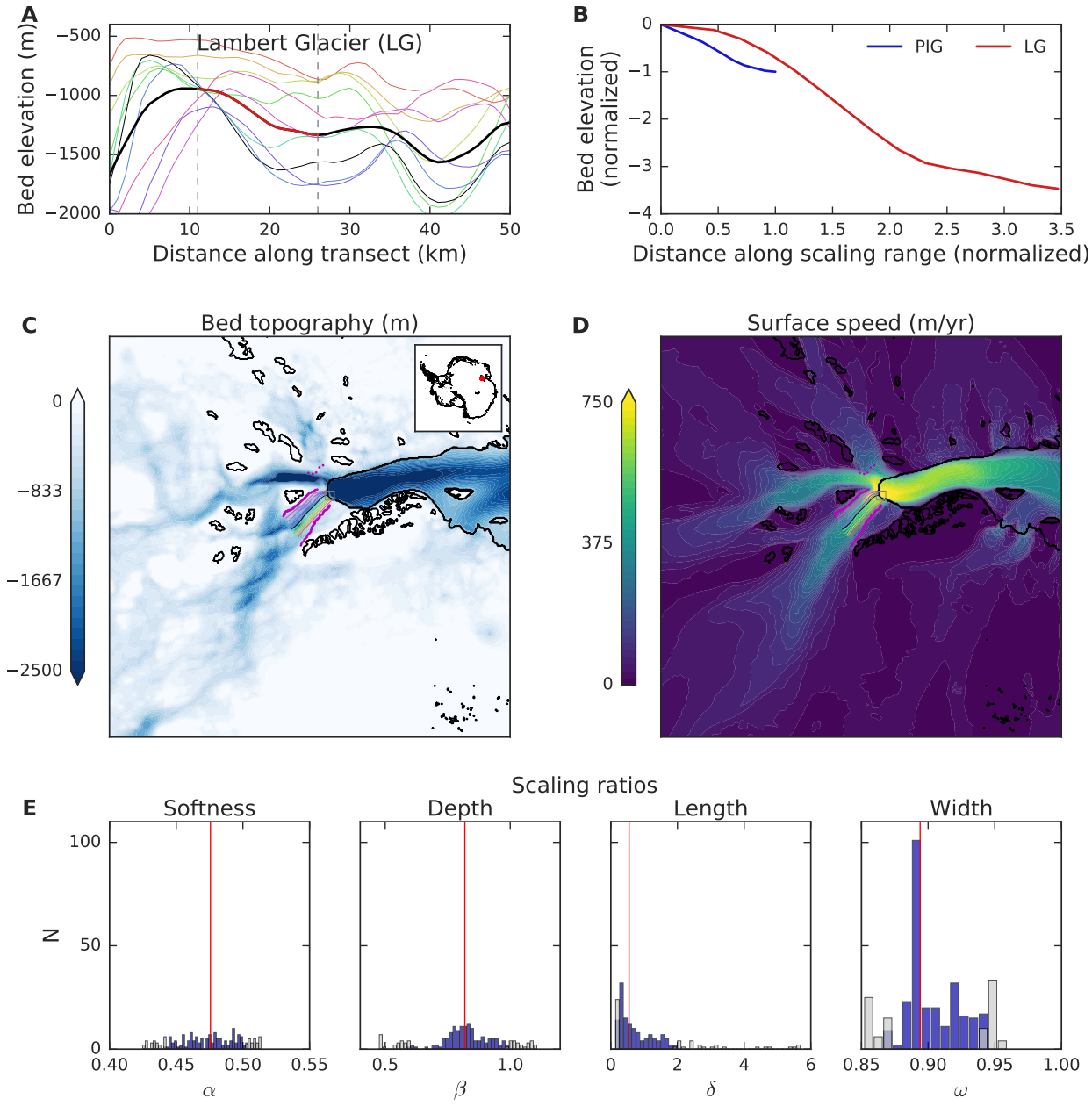

Figure S15. Same as Fig. S10, here for Lambert Glacier (LG).

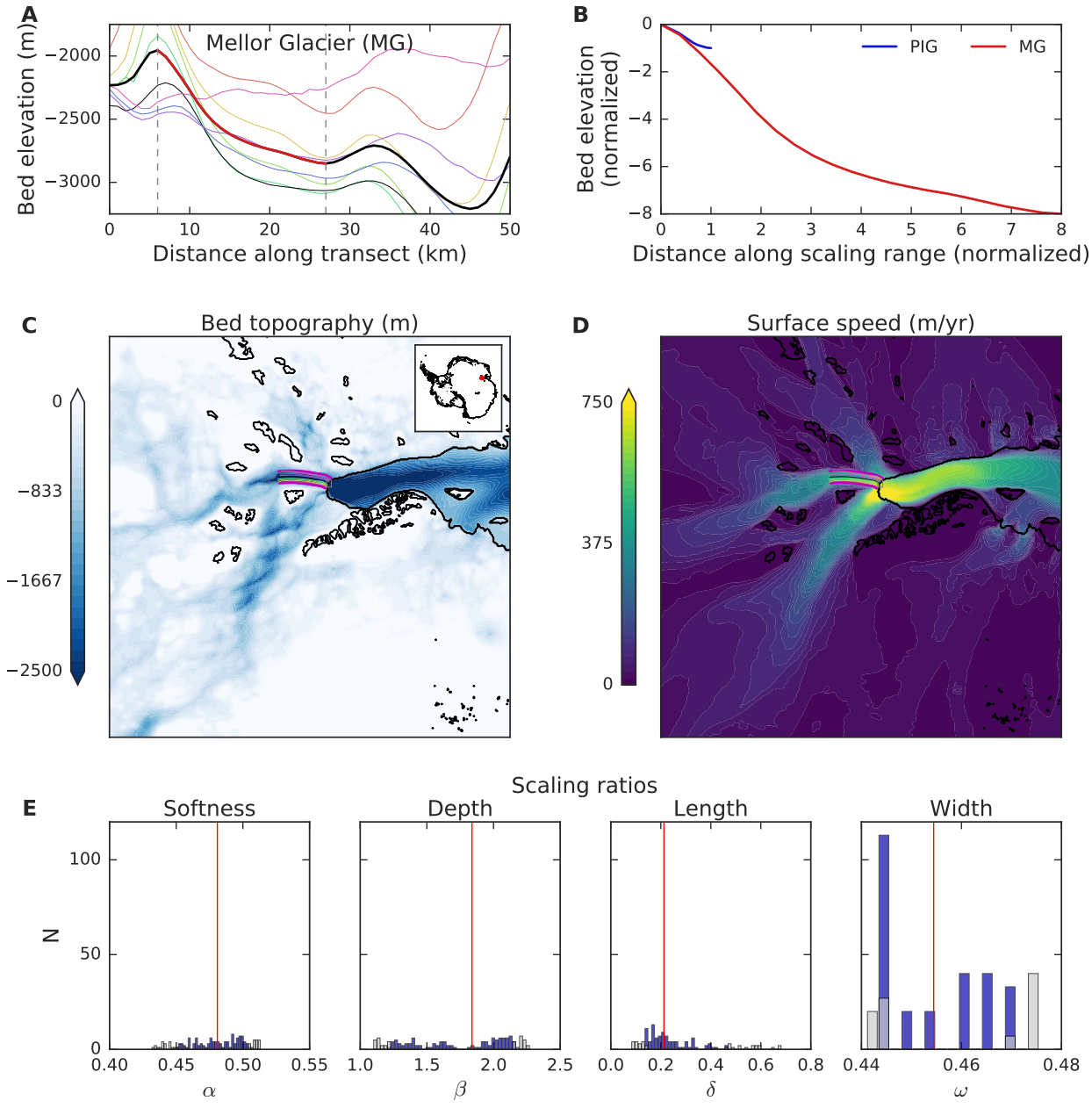

Figure S16. Same as Fig. S10, here for Mellor Glacier (MG).

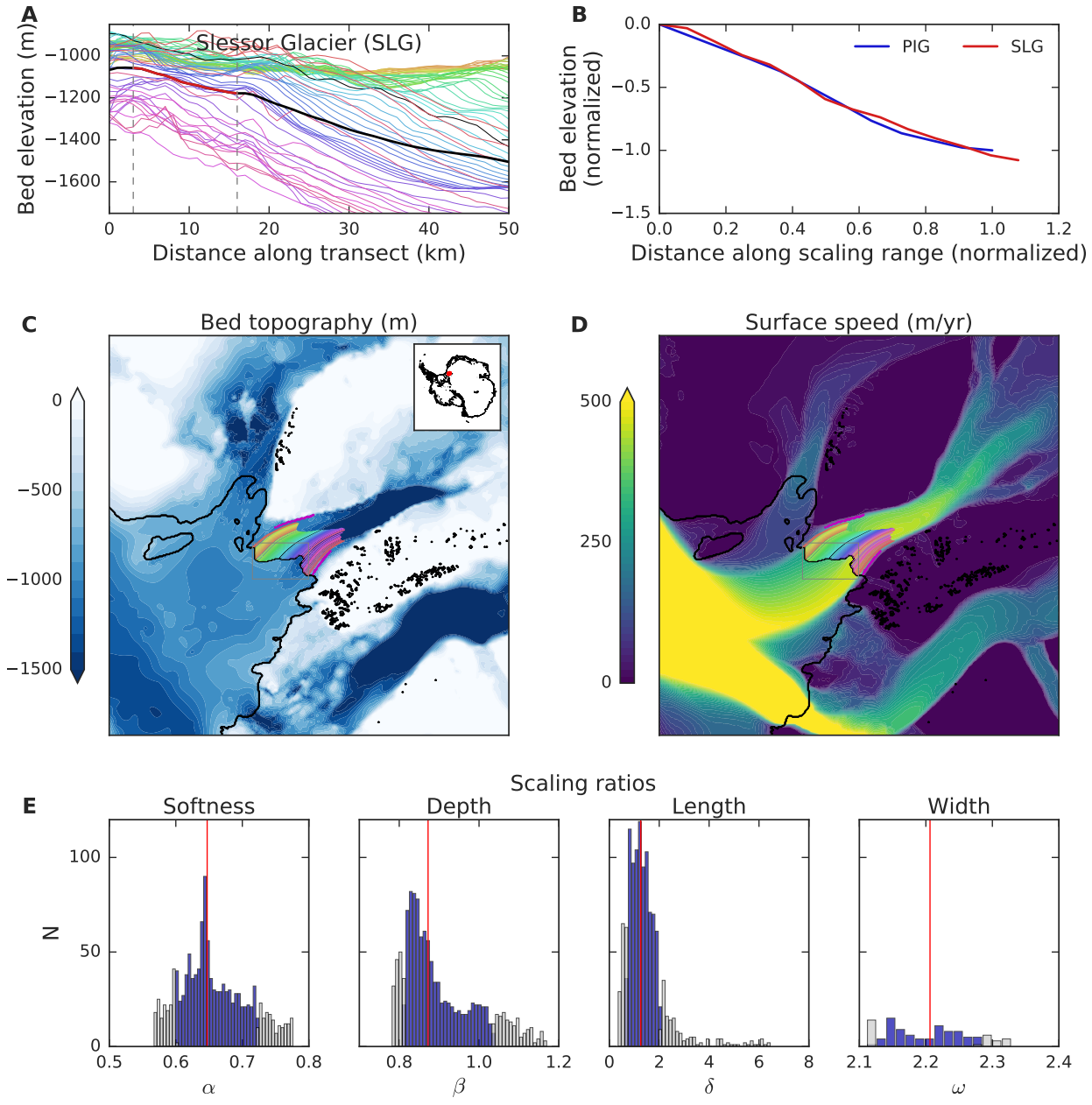

Figure S17. Same as Fig. S10, here for Slessor Glacier (SLG).

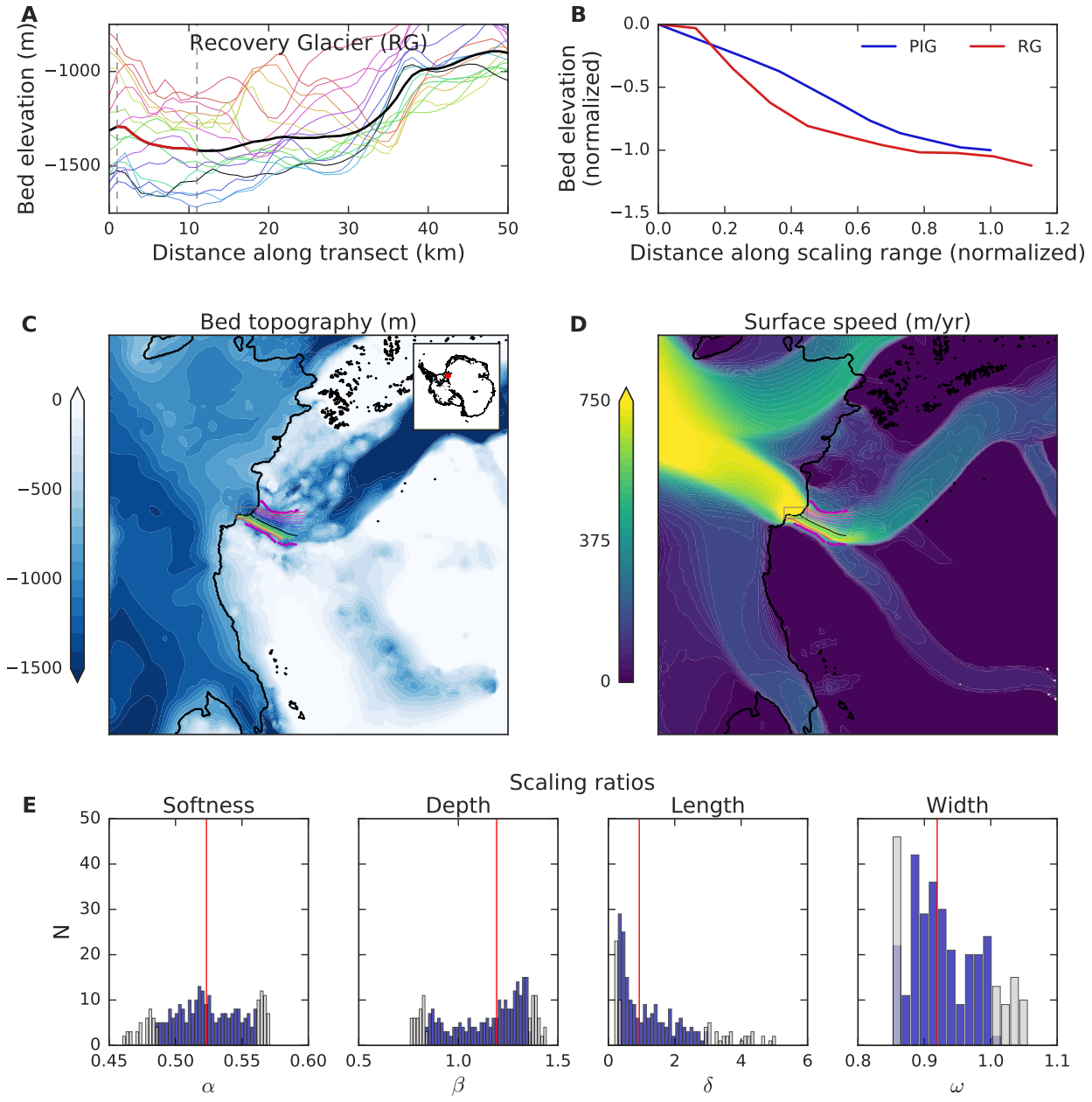

Figure S18. Same as Fig. S10, here for Recovery Glacier (RG).

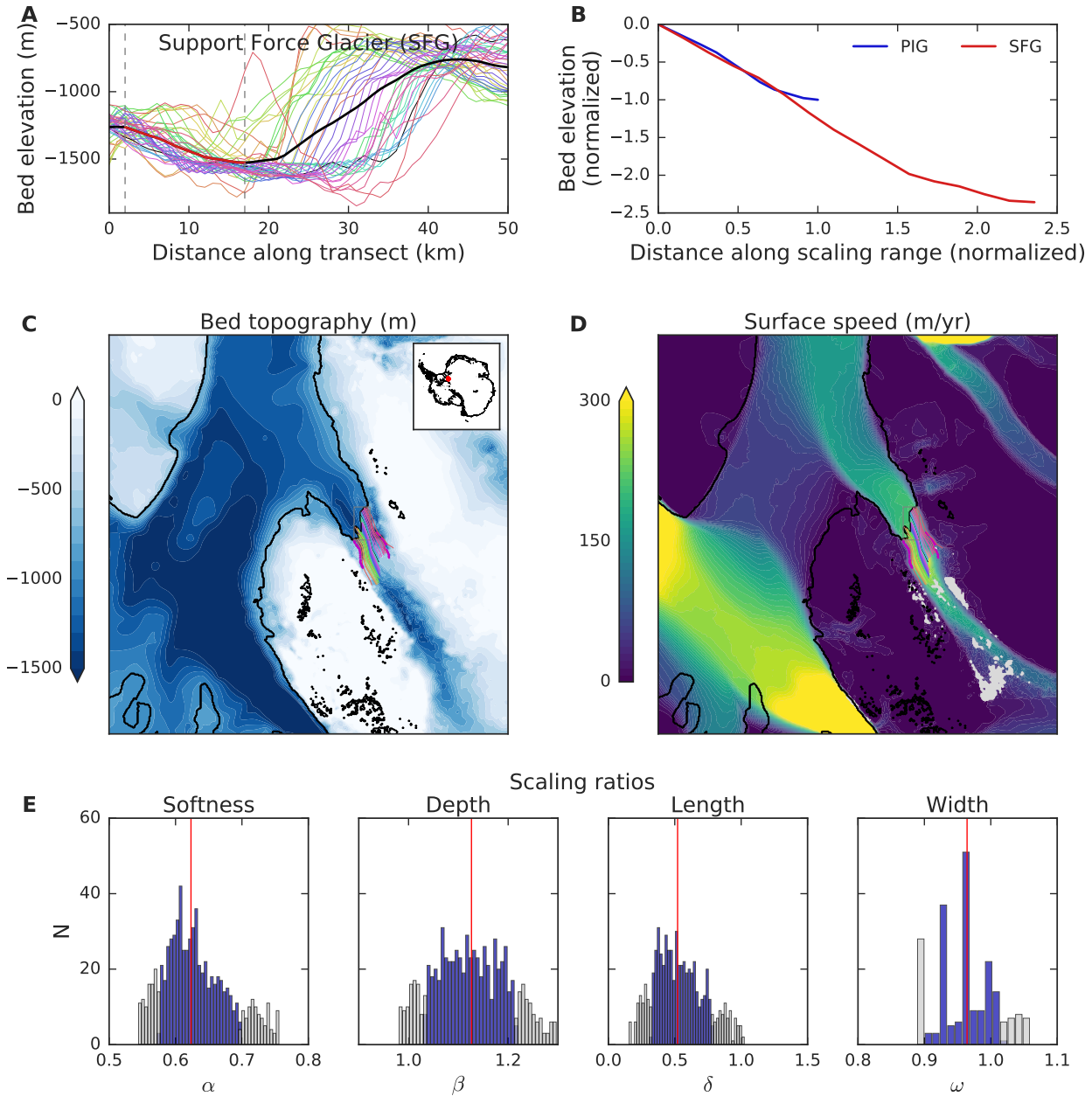

Figure S19. Same as Fig. S10, here for Support Force Glacier (SFG).

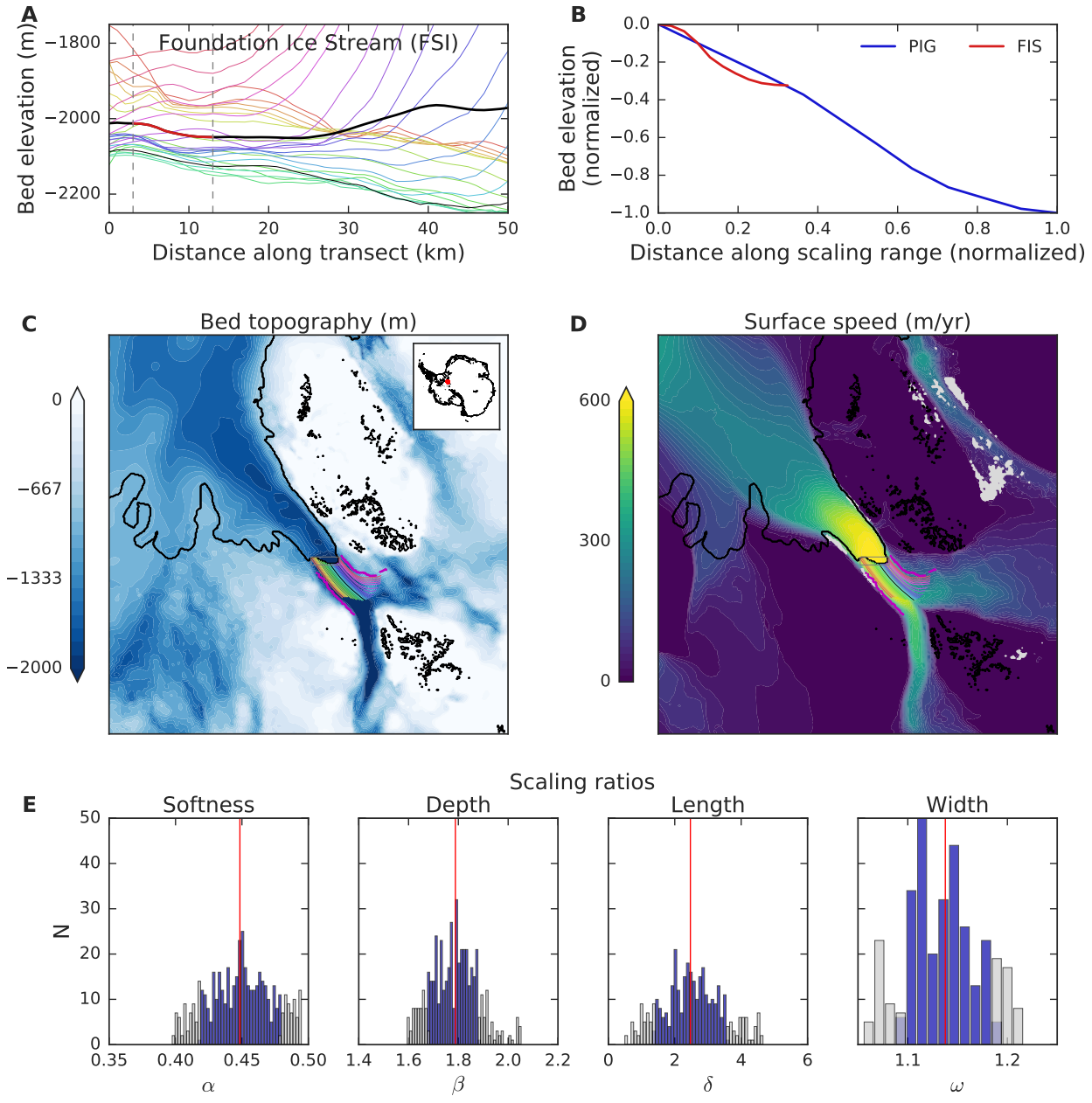

Figure S20. Same as Fig. S10, here for Foundation Ice Stream (FIS).

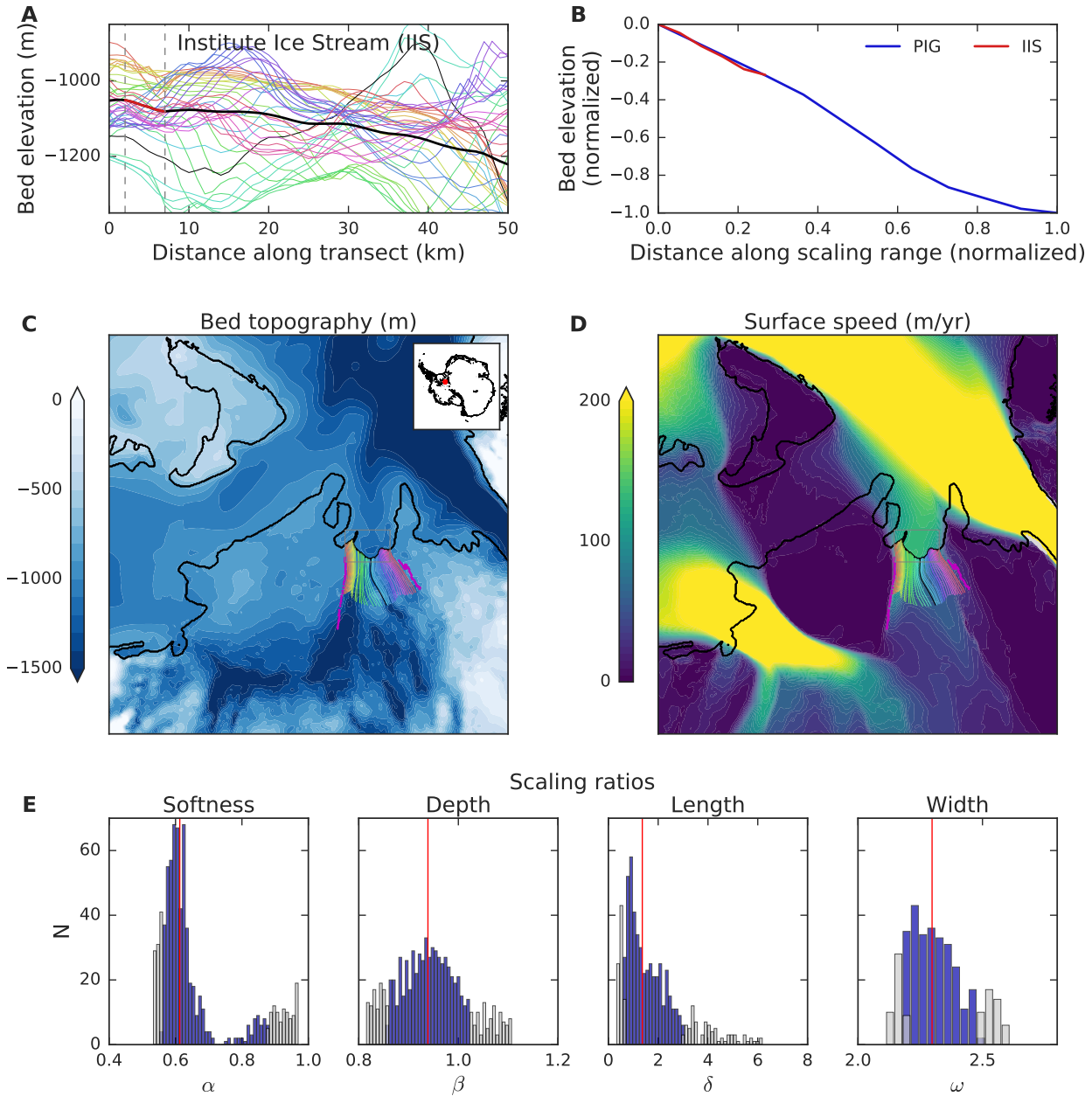

Figure S21. Same as Fig. S10, here for Institute Ice Stream (IIS).

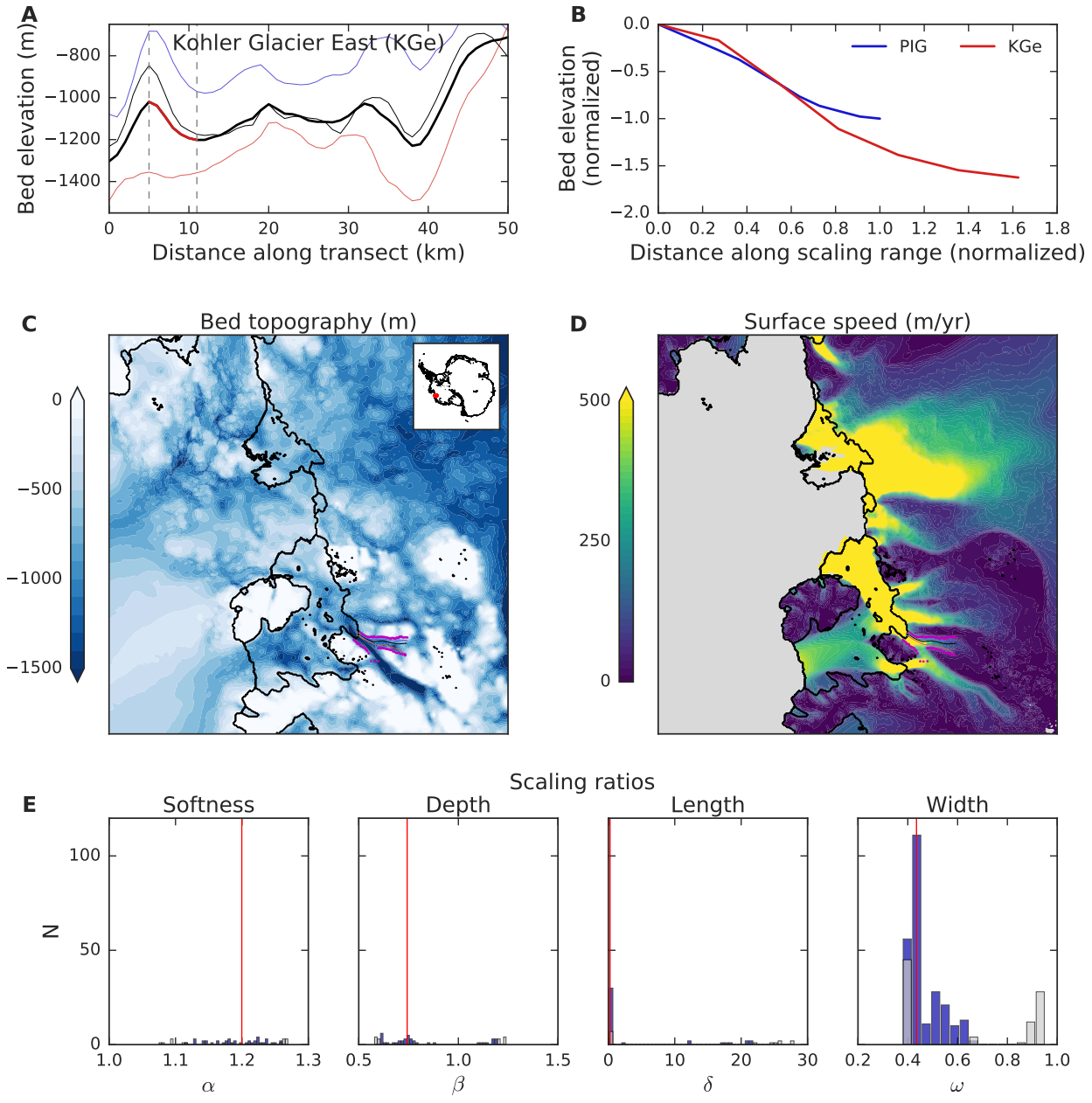

Figure S22. Same as Fig. S10, here for the eastern branch of Kohler Glacier (KGe), which is dicarded in our study.

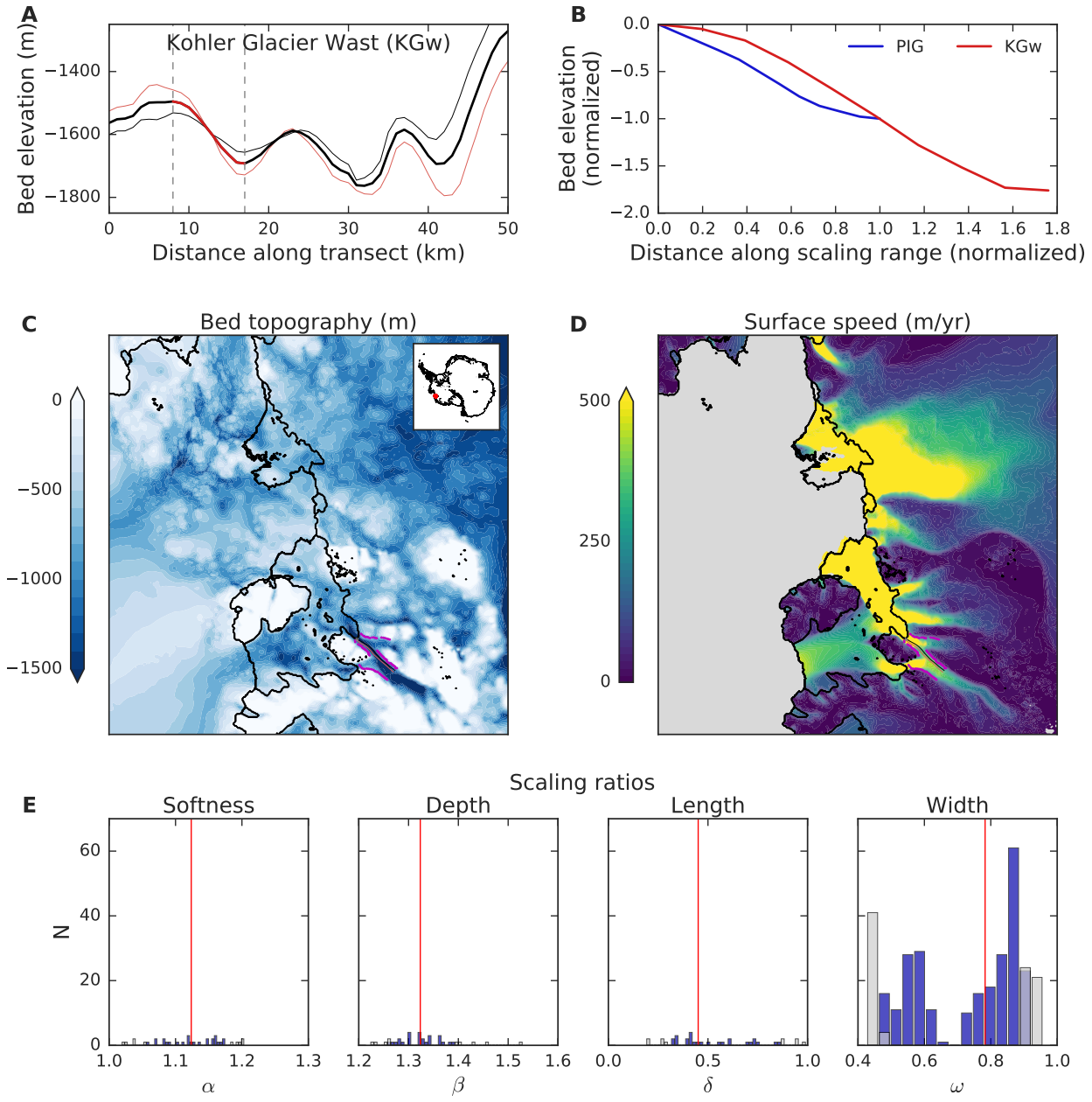

Figure S23. Same as Fig. S10, here for the western branch of Kohler Glacier (KGw), which is dicarded in our study.

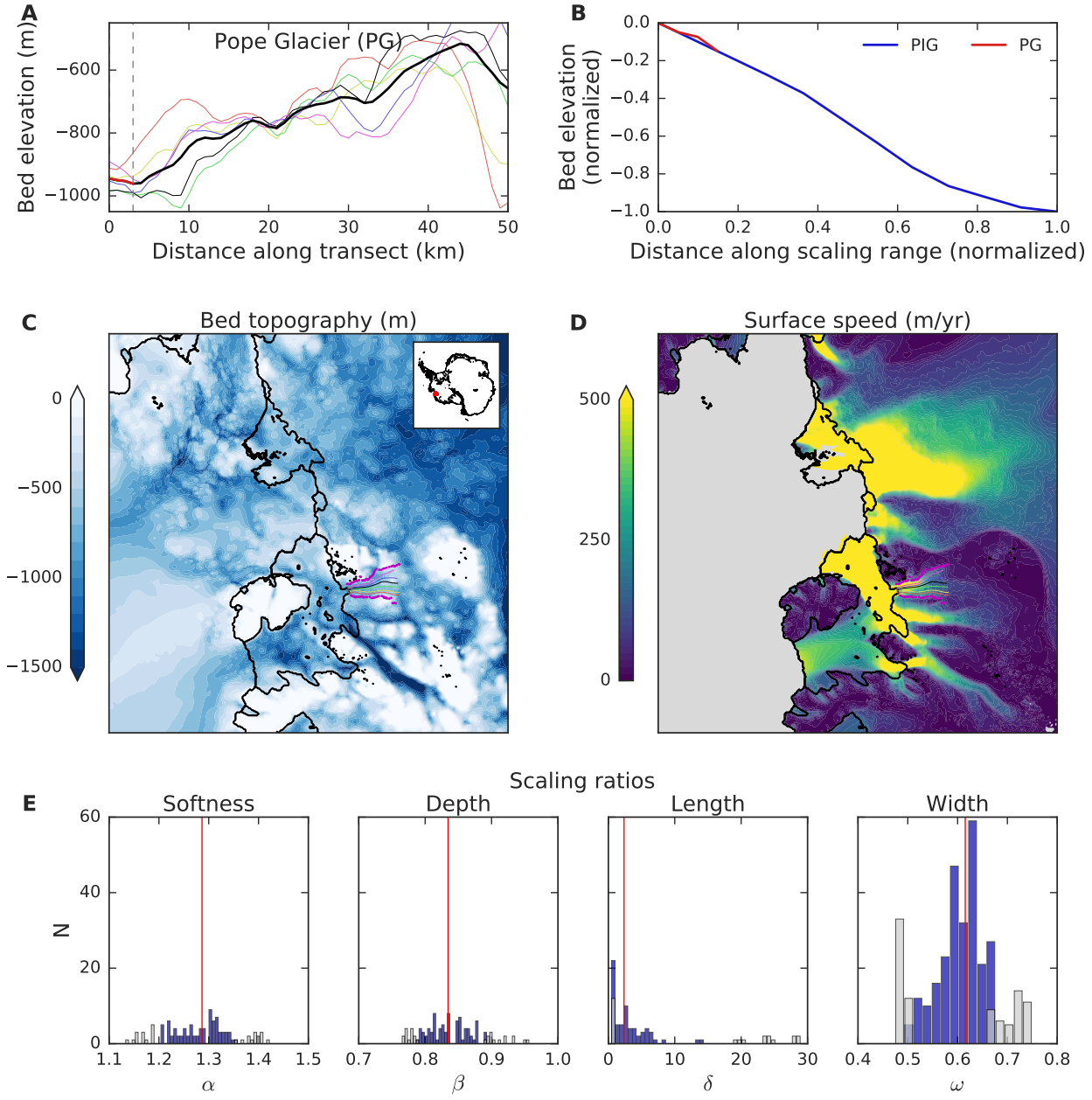

Figure S24. Same as Fig. S10, here for Pope Glacier (PG), which is dicarded in our study.

References

Beckmann, J., Perrette, M., Beyer, S., Calov, R., Willeit, M., and Ganopolski, A.: Modeling the Response of Greenland Outlet Glaciers to Global Warming Using a Coupled Flow Line–Plume Model, The Cryosphere, 13, 2281–2301, https://doi.org/10.5194/tc-13-2281-2019, 2019.

Morlighem, M., Rignot, E., Binder, T., Blankenship, D., Drews, R., Eagles, G., Eisen, O., Ferraccioli, F., Forsberg, R., Fretwell, P., Goel, V., Greenbaum, J. S., Gudmundsson, H., Guo, J., Helm, V., Hofstede, C., Howat, I., Humbert, A., Jokat, W., Karlsson, N. B., Lee, W. S., Matsuoka, K., Millan, R., Mouginot, J., Paden, J., Pattyn, F., Roberts, J., Rosier, S., Ruppel, A., Seroussi, H., Smith, E. C., Steinhage, D., Sun, B., van den Broeke, M. R., van Ommen, T. D., van Wessem, M., and Young, D. A.: Deep Glacial Troughs and Stabilizing Ridges Unveiled beneath the Margins of the Antarctic Ice Sheet, Nature Geoscience, 13, 132–137, https://doi.org/10.1038/s41561-019-0510-8, 2020.

Mouginot, J., Rignot, E., and Scheuchl, B.: Continent-Wide, Interferometric SAR Phase, Mapping of Antarctic Ice Velocity, Geophysical Research Letters, 46, 1–9, https://doi.org/10.1029/2019GL083826, 2019.

Seroussi, H., Nowicki, S., Payne, A. J., Goelzer, H., Lipscomb, W. H., Abe-Ouchi, A., Agosta, C., Albrecht, T., Asay-Davis, X., Barthel, A., Calov, R., Cullather, R., Dumas, C., Galton-Fenzi, B. K., Gladstone, R., Golledge, N. R., Gregory, J. M., Greve, R., Hattermann, T., Hoffman, M. J., Humbert, A., Huybrechts, P., Jourdain, N. C., Kleiner, T., Larour, E., Leguy, G. R., Lowry, D. P., Little, C. M., Morlighem, M., Pattyn, F., Pelle, T., Price, S. F., Quiquet, A., Reese, R., Schlegel, N.-J., Shepherd, A., Simon, E., Smith, R. S., Straneo, F., Sun, S., Trusel, L. D., Van Breedam, J., van de Wal, R. S. W., Winkelmann, R., Zhao, C., Zhang, T., and Zwinger, T.: ISMIP6 Antarctica: A Multi-Model Ensemble of the Antarctic Ice Sheet Evolution over the 21st Century, The Cryosphere, 14, 3033–3070, https://doi.org/10.5194/tc-14-3033-2020, 2020.